SOFC modeling considering hydrogen and carbon monoxide as electrochemical reactants

Andersson, Martin; Yuan, Jinliang; Sundén, Bengt

Published in:
Journal of Power Sources

DOI:
10.1016/j.jpowsour.2012.12.122

2013

SOFC MODELING CONSIDERING HYDROGEN AND CARBON MONOXIDE AS ELECTROCHEMICAL REACTANTS

Martin Andersson*, Jinliang Yuan and Bengt Sundén
Department of Energy Sciences, Faculty of Engineering,
Lund University, Box 118, 221 00 Lund, Sweden

* Corresponding author:
Martin.Andersson@energy.lth.se
+46 46 222 4908 (phone)
+46 46 222 4717 (fax)

ABSTRACT

Fuel cells are promising for future energy systems, because they are energy efficient and able to use renewable fuels. A fully coupled computational fluid dynamics (CFD) approach based on the finite element method, in two-dimensions, is developed to describe a solid oxide fuel cell (SOFC). Governing equations for, gas-phase species, heat momentum, ion and electron transport are implemented and coupled to kinetics describing electrochemical and internal reforming reactions. Both carbon monoxide and hydrogen are considered as electrochemical reactants within the anode. The predicted results show that the current density distribution along the main flow direction depends on the local concentrations and temperature. A higher (local) fraction of electrochemical reactants increases the Nernst potential as well as the current density. For fuel mixtures without methane, the cathode air flow rate needs to be increased significantly to avoid high temperature gradients within the cell as well as a high outlet temperature.

Keywords: *SOFC; Modeling; Hydrogen; Carbon monoxide; Electrochemical reaction mechanisms; Transport processes*

1 INTRODUCTION AND PROBLEM STATEMENT

Fuel cells (FCs) generate electricity and heat via electrochemical reactions (i.e., the reversed electrolysis reactions). There are a variety of designs developed for FCs, but they all operate with the similar basics and principles [1]. FCs are promising candidates for providing electrical power for future energy systems due to the high efficiency and low emissions of NO_x compared to conventional power generation systems [2]. The solid oxide fuel cell (SOFC) operates at temperatures between 600-1000°C [3]. The ability of working at these high temperatures allows SOFCs to operate with different types of fuels no matter they come from a renewable or a fossil, such as methane, methanol, ethanol, gasoline, diesel, syngas, biogas and other oil derivatives [4-6]. Moreover, SOFCs are more tolerant to contaminants than other FCs. In fact, the capability of reforming hydrocarbon fuels promotes SOFCs as prime candidates for leading the transition from conventional power generation with hydrocarbon based fuels to fuel cells which can operate under a wide range of fuels, especially those coming from renewable resources [3].

If hydrogen and/or carbon monoxide are supplied as fuel, no reforming process is required as they can be directly used as electrochemical reactants. Thus, considering hydrogen and carbon monoxide as fuel, the reactions that take place within SOFCs can be globally described as follows: Oxygen is reduced at the cathodic three-phase boundary (TPB), as in eqn (1). The generated oxygen ions are transported through the electrolyte, but the electrons are prevented to pass through it. The electrochemical reactions between hydrogen and oxygen ions, eqn (2), as well as between carbon monoxide and oxygen ions, eqn (3), take place in the anodic TPB [7-8].

$$\frac{1}{2}O_2 + 2e^- \rightarrow O^{2-} \tag{1}$$

$$H_2 + O^{2-} \rightarrow H_2O + 2e^- \tag{2}$$

$$CO + O^{2-} \rightarrow CO_2 + 2e^- \tag{3}$$

When a fuel containing methane is supplied, the reforming reactions take place within the anode. Methane is reformed with steam (eqn (4)), the so-called methane steam reforming reaction (MSR). Carbon monoxide can be oxidized in the electrochemical reaction (eqn (3)) and also react with water (eqn (5)), the so-called water-gas shift reaction (WGSR) [7]. The reactions described here are the overall ones, more detailed reaction mechanisms can be found in [8].

$$CH_4 + H_2O \Leftrightarrow 3H_2 + CO \qquad \text{(MSR, 4)}$$

$$CO + H_2O \Leftrightarrow H_2 + CO_2 \quad \text{(WGSR, 5)}$$

Methane can also react directly with carbon dioxide, according to eqn (6), to produce hydrogen and carbon monoxide. This reaction is called dry reforming (DR) because there is no need of water. Methane can be oxidized according to partial oxidation (POx) in eqn (7) or with total oxidation (FOx) in (8), but also be reformed with steam in the MSR [9-10]. Note that eqns (6)-(8) are not implemented in this work, because it is assumed that the MSR has a significantly higher reaction rate.

$$CH_4 + CO_2 \Leftrightarrow 2H_2 + 2CO \quad \text{(DR, 6)}$$

$$CH_4 + O^{2-} \rightarrow CO + 2H_2 + 2e^- \quad \text{(POx, 7)}$$

$$CH_4 + 4O^{2-} \rightarrow CO_2 + 2H_2O + 8e^- \quad \text{(FOx, 8)}$$

Carbon poisoning is a major concern in SOFCs, when a fuel containing carbon, such as carbon monoxide or methane, is supplied to a Ni anode. The probability for coke formation deepens on the type of fuel, the steam-to-carbon ratio, the catalyst composition and the temperature. Equation (9) describes the Boudouard disproportionation reaction, in which CO is converted into carbon at the catalyst surfaces, lowering the amount of CO available for electrochemical reaction and also causing carbon deposition at the anode surface. CO is reduced using H_2 in eqn (10) to produce carbon and water vapor, contributing to carbon deposition and producing water [11]. The methane cracking is presented in eqn (11) [5]. It is clear that Ni/YSZ anodes are not suitable for direct oxidation of pure CO and the degradation would be rapid [11]. It should be mentioned that eqns (9)-(11) are not considered in our reaction model in the current study. However, carbon poisoning should be considered as the new anode catalysts are designed as well as the operating parameters are decided, in terms of the steam-to-carbon ratio and temperature, to avoid rapid degradation of the cell performance.

$$2CO \rightarrow C + CO_2 \quad (9)$$

$$CO + H_2 \rightarrow C + 2H_2O \quad (10)$$

$$CH_4 \rightarrow C + 2H_2 \quad (11)$$

The electrochemical reactions in SOFC composite electrodes take place in the TPB region, where the electron conducting particles meet with ion conducting particles and also the pores containing gas-phase species. To enable electrochemical reactions the ion and electron conductors must also be in contact with their

corresponding base, i.e., the current collector in case of electron conducting materials and electrolyte in case of ion conducting materials, through other particles of the same type [12]. SOFC electrochemical behavior is mainly determined by the reaction ohmic, activation and concentration polarizations. The respective polarizations are strongly influenced by the microstructure of the electrodes and depend on the quantity and location of the TPBs [13].

Using alternative fuels (compared to hydrogen) gives SOFC a major advantage because pure hydrogen is highly flammable and volatile, which makes it problematic to handle. Additionally hydrogen has low density, which makes storing costly. The price of hydrogen is normally higher, compared to for example natural gas, because hydrogen is not occurring naturally and need to be produced for example through steam reforming of natural gas or coal and sometimes by electrolysis [14]. Syngas and biogas contain a mixture of hydrogen, carbon monoxide as well as other gases and are found to be suitable for direct use in SOFCs. In SOFC modeling, it is common to assume that carbon monoxide is only reformed in the WGSR [15-16], i.e., the electrochemical reaction with carbon monoxide of reactant is neglected. This limitation is released in this paper and the aim is to investigate the impact on the Nernst potential, current density, mole fractions distribution, temperature distribution as well as the WGSR reaction rate within the cell. A parameter study is performed, varying the inlet fuel composition and the air flow rate. The uniqueness of our work besides the coupled hydrogen-carbon monoxide electrochemical approach includes the implementation of the tortuosity factors and the material specific volume fractions for the ion and electron transport within the electrodes as well as the kinetic approach for the WGSR rate, combined with a complete set of simultaneously solved governing equations with the global internal reforming reaction kinetics included.

2 MATHEMATICAL MODEL

A two-dimensional (2D) model for an anode-supported SOFC is developed and implemented in the commercial software COMSOL Multiphysics (version 4.3). Equations for gas-phase species, momentum, ion, electron and heat transport are solved simultaneously. The geometry, based on a standard cell at the Ningbo Institute of Material Technology and Engineering (NIMTE) in China, is defined in Table 1, and a sketch of the investigated cell can be seen in Fig. 1. Note that Fig. 1 is not to scale.

The MINTE cell consists of a 400 μm thick Ni (40%) / YSZ (60%) anode substrate and an active anodic layer of 15 μm, where the electrochemical reactions occur. The electrolyte is a 10 μm thick layer of YSZ. The

cathode consists of a 20 μm thick active layer of LSM/YSZ and a buffer layer of 50 μm LSM. Note that the anode active- and support layers have the same material composition, and the interface may not be very distinct. The major function of the anodic active layer is for the electrochemical reactions at TPBs, while the support layer should enable internal reforming reactions. Since the active region in the anode where the electrochemical reactions take place does not extend too long from the anode–electrolyte interface, a graded porosity can be used to maximize the amount of TPB in the active region. The high mechanical strength is maintained for the rest of the anode which is used primarily as the cell support and for internal reforming reactions, when hydrocarbons are supplied as fuel. The anodic porosity measured is 28 %. The fuel- and air flows are arranged as counter-flows. For the testing, a fuel flow rate of 800 sccm and an air flow rate of 2000 sccm are used. The single cell sample has dimensions of 5·5.8 cm^2, with an active area of 4·4 cm^2. An alumina testing house is used, where the cell temperature is kept constant during the tests, i.e., 750 °C for this case. Voltage probes are placed on the surface of the anode- and cathode support. It should be noted that the NIMTE cell is tested with humidified hydrogen as fuel, compared to partly pre-reformed natural gas as well as different mixtures of hydrogen and carbon monoxide as investigated in the model. The experimental procedures at NIMTE are further described in [17-18].

Table 1: Cell geometry

Cell Component	Thickness
Cell length	0.1 m
Fuel channel height	1 mm
Air channel height	1 mm
Anode thickness	415 μm
Cathode thickness	70 μm
Electrolyte thickness	10 μm
Interconnect thickness	300 μm

2.1 Electron and ion transport

The potential difference between the anode and the cathode current collectors corresponds to the total cell voltage (V_{cell}). The governing equations for the electron and ion transport are implemented as:

$$i_{el} = \nabla \bullet \left(- \sigma_{el,YSZ} \nabla \phi_{el} \right) \tag{12}$$

$$i_{io} = \nabla \bullet \left(- \sigma_{io,Ni/\mathrm{LSM}} \nabla \phi_{io} \right) \tag{13}$$

where σ the ionic/electronic conductivity, i the ion/electron current density, ϕ is the potential, el is the index for the electrolyte material (YSZ) and io for the electron conducting materials (Ni or LSM). The potential at the cathode current collector is set as the cell operating voltage (V_{cell} =0.7 V in this study) and at the anode current collector is set to zero. All other boundaries and interfaces are electrically insulated. The two electrochemical reactions (by H_2 and CO) are treated as two reactions in parallel. Thus, the total local current density for the anode is calculated as the sum of the contributions by carbon monoxide and hydrogen anodic current densities, i.e.:

$$i_c = i_a = i_{a,CO} + i_{a,H_2} \tag{14}$$

Both the Nernst potential and the current density would increase if a pure hydrogen fuel is supplied instead of the different fuel mixtures investigated within this study. However, the aim of this work is to investigate different fuel mixtures containing carbon monoxide as well as study the interaction between the electrochemical reaction with hydrogen and carbon monoxide respectively. The electrochemical reaction with carbon monoxide as reactant corresponds to 15-20 % of the total current, for the fuel compositions tested in this study. However, the impact from neglecting the carbon monoxide direct oxidation path on the total current is higher, due to the strong coupling between the current density, heat generation and local temperature.

The electronic conductivities in the anode and the cathode as well as the ionic conductivity in the electrolyte material are calculated as [19-20]:

$$\sigma_{io,LSM} = \frac{4.2 \cdot 10^7}{T} \cdot \exp\left(\frac{-1200}{T}\right) \tag{15}$$

$$\sigma_{el,YSZ} = 33.4 \cdot 10^3 \cdot \exp\left(\frac{-10300}{T}\right) \tag{16}$$

$$\sigma_{io,Ni} = \frac{9.5 \cdot 10^7}{T} \cdot \exp\left(\frac{-1150}{T}\right) \tag{17}$$

where T is the temperature. The electrons and ions can not be transported in a straight path in the electrodes, because the transport distance increases due to the real/functional material compositions and their micro structures. This is accounted for by using the structure dependent tortuosity factors and volume fractions. The effective ionic and electronic conductivity in the electrodes are defined as [21]:

$$\sigma_{el,ele,YSZ} = \sigma_{el,ele} \cdot \frac{V_{YSZ,e}}{\tau_{YSZ,e}} \tag{18}$$

$$\sigma_{io,a,Ni} = \sigma_{io,a} \cdot \frac{V_{Ni,a}}{\tau_{Ni,a}} \tag{19}$$

$$\sigma_{io,c,LSM} = \sigma_{io,c} \cdot \frac{V_{LSM,c}}{\tau_{LSM,c}} \tag{20}$$

where τ is the tortuosity factors of charge transport and V the volume fraction for the specific materials, as specified in Table 2. Kanno *et al*. calculated (by LBM) the tortuosity factors and the values between 7 and 17 are found for Ni and between 6 and 14 for YSZ, respectively [21]. Iwai *et al*. evaluated the tortuosity factors statistically with the random walk process of nonsorbing particles as well as with the LBM method, and values between 6.91 and 29.46 were found for Ni and between 9.84 and 27.89 for YSZ, respectively, depending slightly on the evaluation methods, but mostly on the direction (x, y and z) [22]. Vivet *et al.* [23] calculated the tortuosity in the range of 3.04 and 6.24 for Ni, and between 1.79 and 2.10 for YSZ, respectively. For this work the dimensionless parameters for the electrode structure stated in Table 2 are employed. It is worthwhile to note that there is an negligible transport of oxygen ions in Ni material and of electrons in YSZ material [23], and therefore it is not considered in this study.

Table 2: Charge Transport properties for the porous electrodes

	V_{YSZ} [24]	V_{Ni} or V_{LSM} [24]	ε_e [24]	τ_{io}	τ_{el}
Anode	0.42	0.28	0.30	10	10
Cathode	0.42	0.28	0.30	10	10

The Nernst potential (E^{Nernst}) is determined by the difference in thermodynamic potentials of the electrode reactions. When a hydrogen-steam mixture is used as fuel, the Nernst potential can be calculated according to eqn (21) [25-26]. The Nernst potential for carbon monoxide as fuel is presented in eqn (23) [27]. It should be mentioned that the expressions for the Nernst potential for hydrogen and for carbon monoxide are developed for simplified pure mixtures, i.e., neither the (local) partial pressure of hydrogen, water or methane influences the Nernst potential for the reaction with carbon monoxide as electrochemical reactant, nor the partial pressure of carbon monoxide, carbon dioxide or methane influence the Nernst potential for the reaction with hydrogen as electrochemical reactant. Suitable Nernst potential expressions specific for more complex fuel mixtures are interesting to be developed in our future models.

$$E_{H_2/O_2}^{Nernst} = E_{H_2/O_2}^{0} - \frac{\mathrm{R}\cdot T}{2\cdot \mathrm{F}}\cdot \ln\left(\frac{p_{H_2O}}{p_{H_2}\sqrt{p_{O_2}}}\right) \tag{21}$$

$$E_{H_2/O_2}^{0} = 1.253 - 2.4516\cdot 10^{-4}\cdot T \tag{22}$$

$$E_{CO/O_2}^{Nernst} = E_{CO/O_2}^{0} - \frac{\mathrm{R}\cdot T}{2\cdot \mathrm{F}}\cdot \ln\left(\frac{p_{CO_2}}{p_{CO}\sqrt{p_{O_2}}}\right) \tag{23}$$

$$E_{CO/O_2}^{0} = 1.46713 - 4.527\cdot 10^{-4}\cdot T \tag{24}$$

where E^0 is the temperature dependent Nernst potential at standard pressure and p_i the partial pressure, at the TPB, in atm. The Nernst potentials are not the same. However, the charge transfer and the mass transfer mechanisms will ensure that the two parallel reaction rates adjust until a single cell potential (V) is obtained, such that [28]:

$$\begin{aligned} V = E_{CO/O_2}^{Nernst} - \eta_{act,a,CO} - \eta_{act,a,O_2} - \eta_{conc,c} - \eta_{conc,a,CO} - i\cdot R = \\ E_{H_2/O_2}^{Nernst} - \eta_{act,a,H_2} - \eta_{act,a,O_2} - \eta_{conc,c} - \eta_{conc,a,H_2} - i\cdot R \end{aligned} \tag{25}$$

where R is the electrochemical resistivity. The activation polarizations are defined as [29-31]:

$$\eta_{act,a,H_2} = \phi_{io} - \phi_{el} - E_{eq,a} \tag{26}$$

$$\eta_{act,c} = \phi_{io} - \phi_{el} - E_{eq,c} \tag{27}$$

$$\eta_{act,a,CO} = E_{CO/O_2}^{Nernst} - E_{H_2/O_2}^{Nernst} + \eta_{act,a,H_2} \tag{28}$$

where the index *a* stands for the anode and *c* for the cathode. Note that eqn (28) is derived from eqn (25) [28]. Notice that the activation polarizations in eqns (26)-(28) are connected to the validated expressions describing the local current density in eqns (46)-(48) (in section 2.5), including, e.g., the local temperature and concentrations. The respectively remarkable source of loss is discussed as the result is presented in section 4.

The concentration polarizations are specified as [32]:

$$\eta_{conc,a,H_2} = \frac{\mathrm{R}T}{n_{e,a}\mathrm{F}}\ln\left(\frac{p_{H_2O,TPB}\cdot p_{H_2,b}}{p_{H_2,TPB}\cdot p_{H_2O,b}}\right) \tag{29}$$

$$\eta_{conc,a,CO} = \frac{\mathrm{R}T}{n_{e,a}\mathrm{F}} \ln\left(\frac{p_{CO_2,TPB} \cdot p_{CO,b}}{p_{CO,TPB} \cdot p_{CO_2,b}} \right) \tag{30}$$

$$\eta_{conc,c} = \frac{\mathrm{R}T}{n_{e,c}\mathrm{F}} \ln\left(\frac{p_{O_2,b}}{p_{O_2,TPB}} \right) \tag{31}$$

where $p_{i,TPB}$ stands for the partial pressure at TPB, $p_{i,b}$ the partial pressure at the interface between the gas channel and the electrode, R is the gas constant, F is the Faraday constant and n_e is the number of electrons transferred per reaction. Note that the expressions for concentration polarizations within the anode do not include methane, neither the influence from carbon monoxide and carbon dioxide in the hydrogen concentration polarization (eqn (29)), nor the influence from hydrogen and water in the carbon monoxide concentration polarization (eqn (30)).

The Nernst potential can also be calculated for the electrochemical reactions with methane (eqns (7)-(8)). However, the Nernst potential differs significantly depending if FOx or POx occurs. The POx gives both a higher voltage and a higher gradient with temperature, compared to the FOx. For a fuel with mostly methane (and neither hydrogen nor carbon monoxide) at the inlet, eqns (2)-(3) start as hydrogen and carbon monoxide becomes available along the main flow direction [10]. The influence from the electrochemical oxidation of methane is neglected within this work, because the electrochemical oxidation rate of methane is neglible, compared to the ones for hydrogen and carbon monoxide. It should be noted that neglecting the electrochemical oxidation of methane is common for models presented within the open literature, such as in [33-34].

2.2 Momentum transport

The gases flow inside the fuel cell components, such as in the fuel and air channels, and in the porous electrodes. Equation (32) is introduced and solved for the gas flow in the fuel and air channels and in the porous materials simultaneously [35-36], i.e., the interface conditions between the gas channels and the porous electrodes do not need to be defined.

$$\left(\frac{\mu}{\kappa} + \rho \cdot \nabla \bullet \vec{\mathrm{u}} \right) \cdot \vec{\mathrm{u}} - \nabla \left[-p + \frac{1}{\varepsilon_p} \left\{ \Psi - \left(\frac{-2}{3} \cdot \mu \right) (\nabla \bullet \vec{\mathrm{u}}) \right\} \right] = \mathbf{F} \tag{32}$$

where κ the permeability of the porous medium ($1.76 \cdot 10^{-11}$ m^2), $\mathbf{F}$ is the volume force vector, Ψ the viscous stress tensor and $\vec{u}$ the velocity vector. The viscosity (μ) and density (ρ) for the participating gas mixtures are evaluated by local mole fractions and temperature, as described in [37].

The gas inlet velocities are defined as a developed laminar flow profile, and the average values are based on the oxygen and fuel utilization, i.e., 12 % and 77 %, respectively, for the case with 30 % pre-reformed natural gas. The fuel flow rate is adjusted to supply the fuel channel with the same amount of hydrogen equivalents (hydrogen and carbon monoxide counts for one and methane for four) for all cases in the parameter study. The air flow rate is adjusted to reach the same outlet temperature for all cases. At the outlets, the pressure is fixed to 1 atm. The relatively low oxygen utilization is applied in this study to limit the temperature gradient within the cell, because the (average) current density is relatively high, due to a high electrochemical active area-to-volume ratio. It should be noted that the extra amount of energy is needed for the air blower, with a low oxygen utilization, with a benefit to the decreased current density gradients along the main flow direction (due to the decreased temperature gradient also along the main flow direction). The authors investigated the influence of a graded electrode structure on the air flow rate (as well as current density distribution) in a recent study [38].

2.3 Gas-phase species transport

In the porous material, there are two kinds of gas-phase species diffusion mechanisms; Knudsen (collisions between the gas molecules and the pore walls) and molecular (collisions between two different gas molecules) diffusions. Knudsen diffusion is important when the mean free path is in the same order or bigger than the pore size, and molecules collide with the solid walls more often than with other molecules. At the SOFC operating temperature of around 1000 K, the mean free path of these gas components is about 0.2-0.5 μm. In this study, the radius of pores is assumed as 0.34 μm, which is of the same order as the mean free path. In other words the Knudsen diffusion should be included in the SOFC models. For a multi-component gas mixture system, the temperature dependent binary diffusion coefficients (D_{ij}) are calculated by the expressions in [39], based on binary-component coefficients of the gases. The Knudsen diffusion coefficient of the component i with the component j in a gas mixture, $D_{k,ij}$, is calculated based on the free molecule flow theory, as described in [40]:

$$D_{k,ij} = \frac{2}{3} \cdot r \cdot \sqrt{\frac{8 \cdot \mathrm{R} \cdot T}{\pi \cdot M_{ij}}} \tag{33}$$

where *r* is the effective radius of the pores. In the porous media, there is an increased diffusion length due to the tortuous paths of connected real pores, and the effective diffusion coefficients are usually corrected by porosity (ε_p) and tortuosity [40-41]:

$$D_{eff,ij} = \frac{\varepsilon_p}{\tau} \cdot \left(\frac{D_{i,j} \cdot D_{k,ij}}{D_{i,j} + D_{k,ij}} \right) \tag{34}$$

Equation (35) is used to describe the gas-phase species transport phenomena for each component inside the cell [36] and solved for the fuel and air channels as well as for the electrodes.

$$\nabla \left(-\rho \cdot w_i \sum_{j \neq i}^{n} D_{eff,ij} \cdot \nabla x_j + \left(x_j - w_j \right) \frac{\nabla p}{p} \bullet \vec{\mathrm{u}} - D_i^T \cdot \frac{\nabla T}{T} \right) + \rho \cdot \vec{\mathrm{u}} \cdot \nabla w_j = S_i \tag{35}$$

In eqn (35) *w* is the mass fraction, *x* the mole fraction of the respective species, *n* the number of species and D_i^T the thermal diffusion coefficient. S_i, the mass source term due to chemical reactions, is defined for the internal reforming and the electrochemical reactions. The eqn (35) is solved for O_2 (and indirectly also for N_2) on the cathode side as well as for ten different pairs of H_2, CO, CO_2, H_2O and CH_4 on the anode side.

The boundary conditions for the outlets are defined as convective fluxes. The cathode inlet is defined as air, including oxygen and nitrogen. The anode inlet conditions are varied in the parameter study and presented in section 3.

2.4 Heat transport

A local temperature equilibrium (LTE) approach is applied, i.e., the temperature is assumed to be locally the same for the gas and solid-phases (within the electrodes). Previously a local temperature non-equilibrium (LTNE) approach has been applied [3]. However, the temperature differences between the phases within the electrodes (where both gas- and solid phases are considered) as well as the difference in overall temperature difference between the inlets and outlets were neglible. The LTE approach is applied to decrease the model complexity and to save computation time. The governing equation for the temperature distribution in this work is defined as:

$$\rho_g \cdot c_{p,g} \cdot \vec{u} \cdot \nabla T = \nabla \bullet \left(k_{eff} \nabla T\right) + Q_h \tag{36}$$

here k_{eff} is the effective thermal conductivity, Q_h the heat generation/consumption (source term defined in eqns (42)-(45)), and $c_{p,g}$ the gas-phase specific heat. Applying a LTE approach means that eqn (36) is valid over the entire model, i.e., no heat transfer coefficients between the solid- and gas phases as well as heat exchange coefficients at the channel walls need to be considered. Note that the overall governing equation for the heat transport reduces to pure heat conduction in the electrolyte and in the interconnector. The effective value of the thermal conductivity in the porous electrodes can be specified as [40]:

$$k_{eff} = \varepsilon_p \cdot k_g + (1-\varepsilon) \cdot k_s \tag{37}$$

where *eff* means effective, *s* solid and *g* gas-phase. The conductivity, the specific heat and the density for the solid materials in the different subdomains are outlined in Table 3.

Table 3: Solid Material Parameters

	Thermal conductivity [42] (W/m/K)	**Specific heat [8]** (J/kg/K)	**Density [8]** (kg/m^3)
Anode (Ni/YSZ)	11	450	3310
Cathode (LSM/YSZ)	6	430	3030
Electrolyte (YSZ)	2.7	470	5160
Interconnect (stainless steel)	20	550	3030

The specific heat for each gas species and the gas mixture is calculated as [43]:

$$c_{p,i} = \sum_{k=1}^{7} \mathrm{a_k} \cdot \left(\frac{T}{1000}\right)^k \tag{38}$$

$$c_{p,g} = \sum_i x_i \cdot c_{p,i} \tag{39}$$

where a_k is the species dependent parameter (extracted from [43]) and "k" stands for the number of parameters involved in the specific heat calculation. The thermal conductivity for each species of the gas-phase, as well as for the gas mixture, is defined as [43]:

$$k_i = 0.01 \cdot \sum_{k=1}^{7} \mathrm{c_k} \cdot \left(\frac{T}{1000}\right)^k \tag{40}$$

$$k_g = \sum_i x_i \cdot k_i \tag{41}$$

where c_k is the species dependent parameter (extracted from [43]) and "k" stands for the number of parameters in the thermal conductivity evaluation.

The heat consumption/generation due to the internal reforming reactions in the anode is implemented by:

$$Q_{h,ref} = r_{ref} \cdot \Delta H_{ref} \tag{42}$$

where r_{ref} is the reaction rate (in mol/m^{3}s) and ΔH_{ref} the enthalpy change of the reforming reactions. The heat generation due to the activation and the concentration polarizations is defined as [20,44]:

$$Q_{h,act+conc} = -\left(\eta_{act,e} + \eta_{conc,e}\right) \cdot i \cdot AV_e \tag{43}$$

The heat generation due to the ohmic polarization is calculated as [20,44]:

$$Q_{h,ohm} = \frac{i_{el}^2}{\sigma_{el}} + \frac{i_{io}^2}{\sigma_{io}} \tag{44}$$

The amount of the heat generated (within the cathode side)/consumed (within the anode side) due to the change of entropy in the electrochemical reactions is defined as [44]:

$$Q_{h,e} = -\Delta S_e \frac{T \cdot i \cdot AV_e}{n_e \cdot \mathrm{F}} \tag{45}$$

where ΔS_e is the entropy change of the electrochemical reactions, calculated from the data in [45] for the anode and the cathode TPBs, respectively.

The boundaries at the top and the bottom of the cell are defined as symmetry conditions, because it is assumed that the cell is surrounded by other ones with identical temperature distribution. The outlet is defined as convective flux and the inlet gas temperature is defined by the operating temperature (1000 K).

2.5 Electrochemical reactions

The current density is calculated separately at the anodic side for hydrogen and carbon monoxide according to the approach developed by Suwanwarangkul *et al.* [31], and presented in eqns (46)-(48). The electrochemical oxidation of methane (eqns (7)-(8)) is neglected, because the electrochemical oxidation rate of methane is neglible, compared to the ones for hydrogen and carbon monoxide [9,27]. Note that this electrochemical

approach also includes the gas-phase partial pressures, which are frequently neglected within the open literature and also in our previous models [3,37,44].

$$i_c = AV_{e,c} \cdot \frac{0.25 \cdot 10^{10} \cdot \exp\left(\frac{-130000}{\mathrm{R} \cdot T}\right) \cdot \mathrm{R} \cdot T \sqrt{p_{O_2}}}{\mathrm{F}} \cdot \left[\exp\left(\frac{-2 \cdot \mathrm{F} \eta_{act,c}}{\mathrm{R} \cdot T} \right) - \exp\left(\frac{2 \cdot \mathrm{F} \eta_{act,c}}{\mathrm{R} \cdot T} \right) \right] \tag{46}$$

$$i_{a,H_2} = AV_{e,a} \cdot \frac{2.1 \cdot 10^{11} \cdot \exp\left(\frac{-120000}{\mathrm{R} \cdot T}\right) \cdot \mathrm{R} \cdot T \cdot p_{H_2O}^{0.266}}{\mathrm{F} \cdot \left(K_{eq,H_2} \cdot p_{H_2}\right)^{0.266}} \cdot \left[\exp\left(\frac{2 \cdot \mathrm{F} \eta_{act,a,H_2}}{\mathrm{R} \cdot T} \right) - \exp\left(\frac{-\mathrm{F} \eta_{act,a,H_2}}{\mathrm{R} \cdot T} \right) \right] \tag{47}$$

$$i_{a,CO} = AV_{e,a} \cdot \frac{0.84 \cdot 10^{11} \cdot \exp\left(\frac{-120000}{\mathrm{R} \cdot T}\right) \cdot \mathrm{R} \cdot T \cdot p_{CO_2}^{0.266}}{\mathrm{F} \cdot \left(K_{eq,CO} \cdot p_{CO}\right)^{0.266}} \cdot \left[\exp\left(\frac{2 \cdot \mathrm{F} \eta_{act,a,CO}}{\mathrm{R} \cdot T} \right) - \exp\left(\frac{-\mathrm{F} \eta_{act,a,CO}}{\mathrm{R} \cdot T} \right) \right] \tag{48}$$

Here K_{eq} the temperature dependent equilibrium constant for eqns (2) and (3), respectively and AV_e is the electrochemically active surface area-to-volume ratio. For AV_e an average value of $9 \cdot 10^6$ m^2/m^3 is applied in this work, which can be compared to $70 \cdot 10^6$ m^2/m^3, the measured specific surface area for Ni/YSZ material developed for SOFC anodes [46]. Note that not all the surfaces are available for the catalytic reactions, due to the distribution of catalysts, unavailable pores and mass transfer limitations among others. The trend for the FC development in recent years has been in the direction of employing smaller pores to get a larger AV. The approach applied in this work (from Suwanwarangkul *et al.* [31]*)* assumes that the pre-exponential factor of the CO oxidation reaction is 2.5 times lower than that of the H_2 oxidation reaction, because the CO oxidation presents a much higher activation polarization than for the H_2 oxidation reaction at the same current density. Also Ni [27] assumes the exchange current density for hydrogen electrochemical reaction to be 2.5 times that for the CO electrochemical oxidation. These assumptions can be compared to the result from Matsuzaki and Yasuda in [47], where it was concluded that the electrochemical oxidation rate of H_2 at the interface in a porous Ni-YSZ cermet electrode and YSZ electrolyte is 1.9-2.3 times higher than that of CO at 1023 K and 2.3-3.1 times higher at 1273 K. O´Brien and Giorgi [11] measured the CO electrochemical oxidation rate on NiCo/YSZ to be approximately three times slower than that of H_2. Note that the difference in oxidation rates between the carbon monoxide and the hydrogen reactions is not the same as the difference in pre-exponential factors or exchange current densities, because the local concentrations and equilibrium constants are included as the current densities are calculated (for this study in eqns (46)-(48)).

2.6 Internal reforming reactions

When a fuel containing methane and carbon monoxide is supplied, the reforming reactions take place within the anode. Carbon monoxide can be oxidized in the electrochemical reaction, but also reacts with water in the WGSR [48]]. Note that the WGSR is in general much faster than the carbon monoxide electrode reaction [47-49]. Methane reacts with steam in the MSR. The DR is neglected due to the relatively high fractions of water in the supplied fuel. The heat, which is generated within the cell (mainly from the electrochemical reactions), can be used for the internal steam reforming reaction within the anode and/or outside the cell for external reforming and pre-heating of the fuel and air. The reaction kinetics from Klein *et al.* [50-51] for the MSR (an Arrhenius form expression dependent on the active area-to-volume ratio) is presented in eqn (49) and used to calculate the reaction rates in this work.

$$r_{MSR} = AV_{MSR} \cdot \left(943 \cdot \exp\left(\frac{-225 \cdot 10^3}{R \cdot T} \right) \cdot p_{CH_4} p_{H_2O} - 7.74 \cdot 10^{-9} \cdot \exp\left(\frac{-1937}{R \cdot T} \right) \cdot p_{CO} p_{H_2}^3 \right) \quad (49)$$

Equation (49) origins from experiments performed at Research Centre Jülish, and the anode material consists of Ni−8YSZ substrate with a standard composition of 50 wt% Ni [50]. For AV_{MSR} an average value of $10 \cdot 10^6$ m^2/m^3 is applied in this work, which can be compared to $70 \cdot 10^6$ m^2/m^3, that is the measured specific surface area for Ni/YSZ material developed for SOFC anodes [46].

Based on the global scheme for the anode, the expression for the catalyzed water-gas shift reaction from Haberman and Young [52] has been selected in this study:

$$r_{WGSR} = k_{WGSR} \cdot \left(p_{H_2O} p_{CO} - \frac{p_{H_2} p_{CO_2}}{K_{WGSR}} \right) \quad (50)$$

The rate constant (k_{WGSR}) and the equilibrium constant (K_{WGSR}) are temperature dependent expressions calculated from the experimental data, as described in [52]. To verify if the WGSR is close to equilibrium or not, the rate constant (k_{WGSR}) is increased 20 times. It is found that the difference in carbon monoxide mole fraction is less than 0.001 at any position at the anode/electrolyte interface for the case with partly pre-reformed natural gas.

3 SOLUTION METHODS AND PARAMETER STUDY

All the equations, defined above, are numerically solved in COMSOL Multiphysics (version 4.3.0.233) using a stationary segregated solver with a direct (MUMPS) linear solver system. The governing equations are segregated in 5 different groups: **1.** velocity field, pressure distribution and pressure corrections, **2.** temperature distribution, **3.** ion and electron distribution, **4.** mass fraction distribution on the air side (O_2/N_2) and **5.** mass fraction distribution on the fuel side ($H_2/H_2O/CH_4/CO/CO_2$). The segregated solver solves for 2 390 000 degrees of freedom and the tolerance is defined to 0.0001 for each segregated group. Grid independence was achieved at 704 000 elements, after which the change (for the standard case with pre-reformed natural gas) in the maximum temperature is less than 0.03 %, in the maximum air velocity less than 0.08 %, in the oxygen consumption less than 0.16 %, in the minimum hydrogen mole fraction less than 0.11 %, in the methane conversion less than 0.21 % and in the average current density less than 0.32 % (compared with the predictions by 1 070 000 elements). It should be noted that the mesh is finest close to the electrode/electrolyte interface and coarsest for the air- and fuel channels and for interconnects. The reason for such a mesh arrangement is mainly due to the fact that the charge transport and the electrochemical reactions (affecting the governing transport equations for ion, electron, mass, heat and momentum) appear only in the regions close to the electrode/electrolyte interface. The calculation time is in the order of several hours on a single computer with 16 GB RAM and a CPU with 3.40 GHz.

Within the parameter study the compositions at the fuel inlet are varied, according to Table 4. The fuel flow rates are specified to ensure that each case supplies the cell with the same amount of fuel, in terms of hydrogen equivalents. The (inlet) air flow rate is adjusted to keep the overall temperature difference between the inlet and the outlet constant. The “dimensionless air flow rate” (listed in Table 4) corresponds to the inlet air velocity relative to the one for the case with 30 % pre-reformed natural gas. Note that some of the cases within the parameter study contain a low steam-to-carbon ratio, i.e., the probability for carbon deposition becomes high close to the fuel inlet. However, this study aims to compare different fuel mixtures in terms of the electrochemical reactions.

Table 4: Parameters changed in the parameter study

Case	x H_2	x CO	x H_2O	x CO_2	x CH_4	Dimensionless air flow rate (-)
30 % pre-reformed natural gas	0.2626	0.0294	0.4934	0.0436	0.171	1.00
1:1:1:1 fuel mixture	0.25	0.25	0.25	0.25	-	1.90
4:4:1:1 fuel mixture	0.40	0.40	0.10	0.10	-	2.70
6:2:1:1 fuel mixture	0.60	0.20	0.10	0.10	-	3.45
2:6:1:1 fuel mixture	0.20	0.60	0.10	0.10	-	2.65

4 SIMULATION RESULTS

The predicted temperature increases along the main flow direction (x-direction), as seen in Fig. 2, for the case with 30 % pre-reformed natural gas as fuel. Heat is produced due to the different polarizations, the change of entropy due to electrochemical reactions in the cathode and the WGSR in the anode. On the other hand, heat is consumed due to the MSR as well as change of entropy due to the electrochemical reaction within the anode. Normally an initial temperature decrease within the anode is expected as partly pre-reformed natural gas is supplied as fuel. However, this is not the case within this study, since a relatively low inlet temperature is applied together with a quite low inlet fraction of methane as well as a relatively high electrochemical active area-to-volume ratio, which gives a (initial) significant heat generation from the high current density. A temperature difference is predicted in the y-direction inside the air channel because the convective heat flux in the air channel is bigger compared to the one in the fuel channel due to the relatively larger mass flow rate. An increased cell temperature increases the cell current density. However, a too high temperature gradient or maximum temperature decreases the life length of the cell, due to material degradation and failure. The current density increases along the main flow direction mainly due to an increased cell temperature. The increase is limited because of the decrease in Nernst potential due to the temperature increase and the consumption of electrochemical reactants along the main flow direction. The pressure drop for the case with 30% pre-reformed natural gas is about 20 Pa on the anode side and 140 Pa on the cathode side.

The current density distribution along the y-direction (i.e., the direction normal to the main flow direction), at the inlet and outlet, in the cathode (to the left), electrolyte and anode (to the right) can be seen in Fig. 3 and along the x-direction (i.e., the main flow direction) in Fig. 4. Note that for the anode and cathode, only the parts (20 μm) closest to the electrolyte interface are included in Fig. 3. The depth or thickness of the TPB region (in the direction normal to the main flow direction) is 1.0 μm for the cathode side, and 2.6 μm for the anode side. The thickness is defined as the region where 90 % of the electrochemical reactions occur. It is concluded that the current density gradients are steeper on the cathode side than on the anode side. The depth of the active

electrochemical reaction zones is quite small compared to the designed active layers (for example, 20 and 15 μm for the cathode and anode, respectively, for the NIMTE standard cell). The current density increases along the main flow direction as the as the exchange current density increases due to the increased temperature. The increase in current density is limited, due to the decreased Nernst potential, caused by the temperature increase along the main flow direction. The ohmic resistance decrease from an increased temperature. It should be noted that also the consumption of electrochemical reactants and the generation of electrochemical products along the main flow direction decreases the Nernst potential.

The potential distribution is shown in Fig. 5 for the positions close to the inlet and the outlet. The ideal voltage decreases along the flow direction due to both the temperature increase as well as the consumption of fuel and oxygen. It can be revealed from Fig. 5 that 54 % and 48 % of the polarizations occur in the anode at the inlet and outlet, respectively, 22 % and 25 % in the electrolyte at the inlet and outlet, respectively, as well as 24 % and 27 % in the cathode at the inlet and outlet, respectively. The difference in the respective polarizations between different positions can be explained by the temperature distribution and the increased ohmic polarization due to the increased current density along the main flow direction. It should be noted that the relationship between the current density and voltage, the so-called I-V curve, changes along the main flow direction as the cell operating conditions evolve.

The Nernst potential varies along the main flow direction, as presented in Fig. 6 for the case with 30 % pre-reformed natural gas as fuel. The Nernst potential for hydrogen and for carbon monoxide as electrochemical reactants are not the same. However, the charge transfer and the mass transfer mechanisms will ensure that the two parallel reaction rates adjust until a single cell potential (V) is obtained, according to eqn (25). For this case the Nernst potential concerning the electrochemical reaction with carbon monoxide as reactant and carbon dioxide as product are slightly lower, compared to the electrochemical reaction with hydrogen as reactant and water as product. It is advantageous to increase the Nernst potential, because a higher current density can be achieved with the same operating voltage and temperature. The Nernst potential can be increased from a decreased temperature, a decreased mass transport resistance through the electrodes, an increased fraction of electrochemical reactants or a decreased fraction of electrochemical products. The Nernst potential decreases along the main flow direction, due to the increased temperature, decreased concentration of electrochemical reactants and the increased concentration of electrochemical products.

The overall results are presented in Table 5. It should be noted that the fuel flow rate is adjusted to supply the fuel with the same amount of hydrogen equivalents (hydrogen or carbon monoxide counts for one and methane for four) for all cases in the parameter study. Air utilizations of 4-5 % may not be reasonable for commercial fuel cell operation. However, in this study the air flow rate is adjusted to reach the same outlet temperature for all cases, which gives very low oxygen utilizations, because the current density is relatively high. It is clear there are advantages to supply the cell with natural gas (strongly endothermic reforming reaction) in terms of the amount of supplied air. Fuel utilizations around 90 % result in a low Nernst potential close to the outlet, i.e. high current density gradients along the main flow direction

Table 5: Overall results

Case	Average current density (A/m^2)	Fuel utilization	Air utilization	Average inlet fuel velocity (m/s)	Average inlet air velocity (m/s)	Operating Voltage (V)
30 % pre-reformed natural gas	8250	77 %	12 %	0.198	2.52	0.70
1:1:1:1 fuel mixture	8700	85 %	5 %	0.386	4.78	0.70
4:4:1:1 fuel mixture	10250	90 %	4 %	0.241	6.79	0.70
6:2:1:1 fuel mixture	10750	86 %	5 %	0.241	8.68	0.70
2:6:1:1 fuel mixture	9900	91 %	4 %	0.241	6.67	0.70

The current density (Fig. 7) increases when a fuel containing a 1:1:1:1 fuel mixture of hydrogen, carbon monoxide, water and carbon dioxide is supplied, compared to the case with pre-reformed natural gas, due to the higher fraction of electrochemical reactants close to the inlet. The average current density is 8700 A/m^2, compared to 8250 A/m^2 for the case with pre-reformed natural gas. However, the difference between the maximum current densities is bigger, 10500 A/m^2, compared to 9600 A/m^2. The hydrogen Nernst potential (Fig. 8) at the inlet is increased (to 0.964 V) from an increased TPB fraction of hydrogen. However, at the outlet the hydrogen Nernst potential is decreased (to 0.795 V), compared to the case with pre-reformed natural gas (with a hydrogen Nernst potential of 0.942 V at the inlet and of 0.842 V at the outlet), due to a decreased mole fraction of hydrogen. The mole fraction distribution along the main flow direction, at the TPB, for the case implementing a 1:1:1:1 mixture of hydrogen, carbon monoxide, water and carbon dioxide as inlet fuel composition is presented in Fig. 9. Hydrogen and carbon monoxide are consumed in the electrochemical reactions and consequently water and carbon dioxide are generated along the main flow direction. Carbon monoxide has a slighter higher mole fraction than hydrogen at the outlet, because the equilibrium condition of the WGSR. The difference at the inlet between the mole fractions within the fuel channel (0.25 for all participating species) and

the TPB (as presented in Fig. 9) are due to the gas-phase mass transfer resistance within the anode coupled to the WGSR. Le Chatelier's principle tells that the equilibrium constant for the WGSR decreases as the temperature increases along the main flow direction, because this reaction is exothermic. A decreased equilibrium constant means that the equilibrium proceeds towards the left, i.e., producing carbon monoxide and water (from hydrogen and carbon dioxide). For the WGSR the pressure has no effect on the equilibrium constant, because the products and reactants have the same number of moles within the reaction. Since the electrochemical reaction with hydrogen as reactant corresponds to 80-85 % of the current on the anode side, the WGSR is pushed proceeds towards the right producing additional hydrogen (and consuming carbon monoxide), i.e., opposite to the impact from the increased temperature along the main flow direction." It should be mentioned that the fuel utilization is higher as the 1:1:1:1 fuel mixture is supplied, compared to the case with pre-reformed natural gas. However, the same amount of fuel, in terms of hydrogen equivalents, is supplied. Notice, the air flow rate is increased with a factor of 1.9 to compensate for the loss of cooling from the internal reforming reactions (to keep the outlet temperature constant), i.e., the electricity consumption in the air pump increases significantly and also the area required for heat transfer between the ingoing and outgoing streams has to be increased, compared to the case with 30 % pre-reformed natural gas.

The average current density increases to 10250 A/m^2 (Fig. 10) as a 4:4:1:1 fuel mixture of hydrogen, carbon monoxide, water and carbon dioxide is supplied. The current density is lower at the outlet compared to that at the inlet due to the low fractions of the electrochemical reactants at the TPB at the outlet, i.e., due to the high fuel utilization. The Nernst potential (Fig. 11) for both the reactions with hydrogen as well as carbon monoxide as fuels are increased throughout the cell, with the biggest increase at the inlet (1.021 V for carbon monoxide and 1.017 V for hydrogen), compared to both the case with pre-reformed natural gas (0.942 V for carbon monoxide and 0.938 V for hydrogen) as well as the one with a 1:1:1:1 fuel mixture (0.969 V for carbon monoxide and 0.964 V for hydrogen). This increase can be explained from the high (inlet) fractions of hydrogen and carbon monoxide as well as low fractions of water and carbon dioxide. An increased Nernst potential results in an increased activation polarization (with a constant cell voltage), i.e., the current density increases.

The fuel at the inlet consists of a 2:6:1:1 mixture of hydrogen, carbon monoxide, water and carbon dioxide, which gives an average current density of 9900 A/m^2 (Fig. 12). The current density decreases due to a lower Nernst potential (Fig. 13) as well as a lower hydrogen fraction at the TPB. The relatively low current density

close to the outlet can be explained from low concentrations of electrochemical reactants, i.e., a high fuel utilization. The Nernst potential decreases along the flow direction because the temperature increases, the electrochemical reactant fraction decreases and the electrochemical product fraction increases. The difference between the Nernst potential at the inlet and at outlet is bigger for this case (0.215 V) compared to previous cases (for example 0.099 V for the case with pre-reformed natural gas and 0.17 V for the 1:1:1:1 mixture), due to an increased difference between the electrochemical reactant fractions at the inlet and at the outlet. Note that the carbon monoxide mole fraction decreases from 0.60 in the fuel channel to 0.47 at the TPB at the inlet (Fig. 14), mainly due to the WGSR within the anode. The WGSR rate (Fig. 15) decreases along the main flow direction, from 15 mol/m^3/s close to the inlet to zero close to the outlet. The electrochemical reaction rate for the reaction with hydrogen as fuel is faster, compared to the one with carbon monoxide as fuel, because the activation polarization for carbon monoxide corresponds to a lower current density, compared to hydrogen.

The highest average current density (from the cases presented within this work) corresponds to the case with the highest concentration of hydrogen, i.e., the 6:2:1:1 mixture of hydrogen, carbon monoxide, water and carbon dioxide, which gives an average current density of 10750 A/m^2 (Fig. 16). The current density is 9800 A/m^2 at the inlet, due to the high concentration of hydrogen as well as the high Nernst potential (Fig. 17). The WGSR rate (Fig. 18) increases along the main flow direction, from -15 mol/m^3/s close to the inlet to around 15 mol/m^3/s close to the outlet, because the electrochemical reaction with hydrogen is faster than the one with carbon monoxide. Note that the reaction proceeds backwards in the region close to the inlet, because the conditions (temperature and concentrations) are far from equilibrium, i.e., carbon monoxide and water are produced from hydrogen and carbon dioxide. Note that there is some local heat consumption as the WGSR proceeds backwards. As hydrogen is consumed along the main flow direction, in both the WGSR and the electrochemical reaction, the reaction turns forwards and starts to produce hydrogen from carbon monoxide.

5 CONCLUSIONS

A CFD approach is developed and implemented to analyze various physical and chemical phenomena, which take place inside a single cell of an anode-supported SOFC. Equations for momentum, gas-phase species, heat, ion and electron transport are solved simultaneously and couplings with kinetic expressions for electrochemical and internal reforming reactions appearing in various domains are considered. Both carbon monoxide and hydrogen are included as the reactants in the electrochemical reactions within the anode. The

electrochemical reactions are defined in a finite region close to the electrode/electrolyte interface and implemented as specific source terms in the governing transport equations. The activation polarization for the electrochemical reaction with hydrogen as reactant and the one with carbon monoxide as reactant does not correspond to the same current density, i.e., the two electrochemical reactions are treated as two individual ones in parallel and the total current density for the anode is the sum of the two.

The usage of a fuel without methane increases the need of air significantly, in order to keep the outlet temperature constant, compared to the case with pre-reformed natural gas. The increased need for cooling is due to the lack of the heat consumed by MSR and also that the current density is increased. An increased air flow rate gives an increased internal electricity consumption due to the air pump and also increased heat transfer areas between the ingoing and outgoing streams. Consequently, it is important to include the operating condition when the fuel cell system is designed. For the case with an initial low concentration of carbon monoxide, the WGSR proceeds backwards in the region close to the inlet, because the local conditions are far from equilibrium. It is concluded that the WGSR within the anode results in high mole fraction gradients through the anode in the direction normal to the main flow direction.

The current density distribution along the main flow direction depends mainly on the Nernst potential, the temperature as well as and the distribution of the electrochemical reactants and products. The temperature and the fractions of electrochemical products increase along the main flow direction. The Nernst potential and the fractions of electrochemical reactants decrease along the main flow direction. It is found that a fuel mixture containing a high fraction of electrochemical reactants (hydrogen and carbon monoxide) enables a high Nernst potential in the region close to the inlet, which increases the current density at the inlet. On the other hand, a fuel mixture including methane, i.e., with internal reforming within the cell, produces electrochemical reactants and consumes electrochemical products along the main flow direction, resulting in a decreased Nernst potential gradient along the main flow direction. The Nernst potential covering the electrochemical reaction with carbon monoxide has a stronger influence from changes in the operating temperature, compared to the reaction with hydrogen. The fact that the electrochemical reaction with hydrogen corresponds to a higher current density is also the reason for an increased average current density for the cases with a high hydrogen mole fraction at the fuel inlet. It is important to note that the expressions describing Nernst potential for the electrochemical reaction with hydrogen as well as for carbon monoxide are developed for “pure” mixtures.

6 NOMENCLATURE

AV	surface area-to-volume ratio, $m^2\ m^{-3}$
c_p	specific heat at constant pressure, $J\ kg^{-1}K^{-1}$
D_{ij}	Maxwell-Stefan binary diffusion coefficient, $m^2\ s^{-1}$
$D_{k,ij}$	Knudsen diffusion coefficient, $m^2\ s^{-1}$
D_i^T	thermal diffusion coefficient, $kg\ m^{-1}s^{-1}$
E	(actual) operating voltage, V
E^0	open circuit voltage at standard pressure, V
F	volume force vector, $N\ m^{-3}$
F	Faraday constant, 96485 $C\ mol^{-1}$
ΔH	enthalpy change of reaction, J/mol
i	volume current density, $A\ m^{-3}$
k	thermal conductivity, $W\ m^{-1}\ K^{-1}$, rate constant, -
K_{eq}	equilibrium constant
n	number of species, -
n_e	number of electrons transferred per reaction, -
p	pressure, Pa or atm
Q_h	source term (heat), $W\ m^{-3}$
R	gas constant, 8.314 $J\ mol^{-1}K^{-1}$
R	electrochemical resistivity, $\Omega \cdot m$
r	average particle/pore radius, m, reaction rate, $mol/(m^3 \cdot s)$
ΔS	entropy change of reaction, J/(K·mol)
S_i	source term (mass), $kg\ m^{-3}s^{-1}$
T	temperature, K
$\vec{u}$	velocity vector, $m\ s^{-1}$
w_i	mass fraction of species i, $kg\ kg^{-1}$
x, y	coordinate system, m
x_j	molar fraction of species j, $mol\ mol^{-1}$

6.1 Greek symbols

Ψ	viscous stress tensor, $N\ m^{-2}$

ϕ potential, V

ε_p porosity, -

η polarization, V

κ permeability, m^2

μ dynamic viscosity, Pa s

ρ density, kg m^{-3}

σ ionic/electronic conductivity, $\Omega^{-1}m^{-1}$

τ tortuosity, -

6.2 Subscripts and superscripts

a anode

act activation

b electrode/gas channel interface

c cathode

conc concentration

e electrode, $e \in \{a, c\}$, electrochemical

E_{eq} equilibrium voltage (V)

eff effective

el electrolyte material

ele electrolyte

g gas-phase

i molecule i

io electrode material

j molecule j

Nernst Nernst potential

ohm ohmic

s solid-phase

6.3 Abbreviations

DR dry reforming reaction

FC fuel cell

FOx	total oxidation reaction
LTE	local temperature equilibrium
LTNE	local temperature non-equilibrium
IEA	International Energy Agency
MUMPS	MUltifrontal Massively Parallel sparse direct Solver
MSR	methane steam reforming reaction
NIMTE	Ningbo Institute of Material Technology and Engineering, China
POx	partial oxidation reaction
SOFC	solid oxide fuel cell
TPB	three-phase boundary
WGSR	water-gas shift reforming reaction

6.4 Chemical

C	carbon (coke) formation at the catalytic surface
CH_4	methane
Co	cobalt
CO	carbon monoxide
CO_2	carbon dioxide
e^-	electron
H_2	hydrogen
H_2O	water
LSM	lanthanum strontium manganite
N_2	nitrogen
Ni	nickel
NO_x	nitrogen oxides
O^{2-}	oxygen ion
O_2	oxygen
YSZ	yttria-stabilized zirconia

7 ACKNOWLEDGMENT

The financial support from the European Research Council (ERC-226238-MMFCs) and the Swedish Research Council (VR-621-2010-4581) are gratefully acknowledged.

LIST OF FIGURES

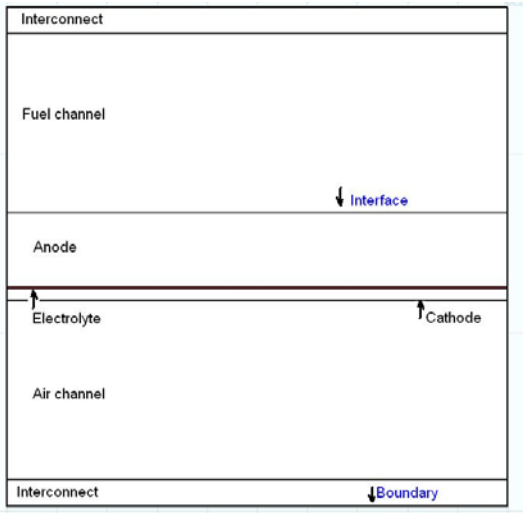

Figure 1: Sketch of an anode-supported SOFC, not to scale.

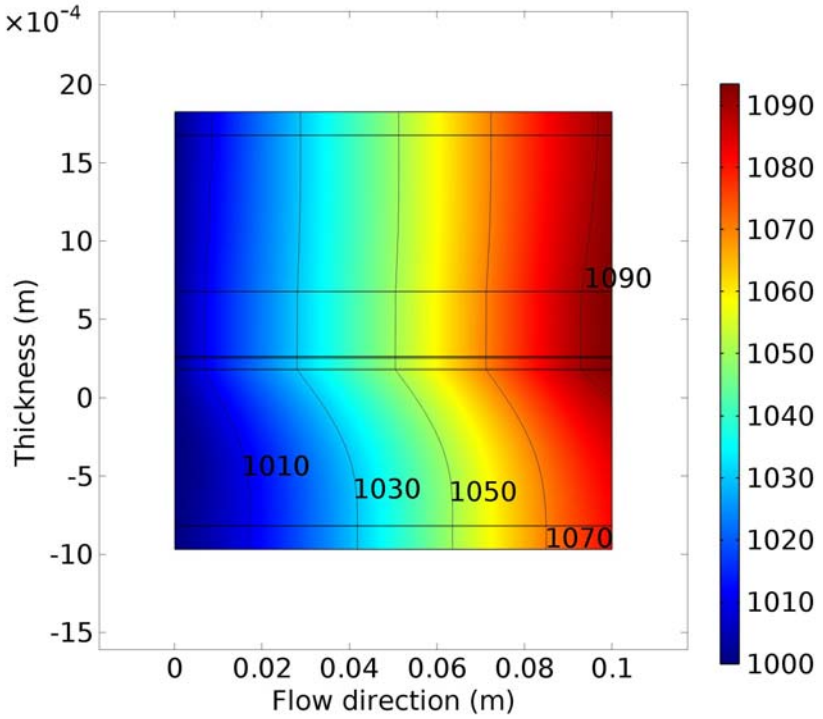

Figure 2: Temperature distribution (in K) for the case with 30 % pre-reformed natural gas as fuel.

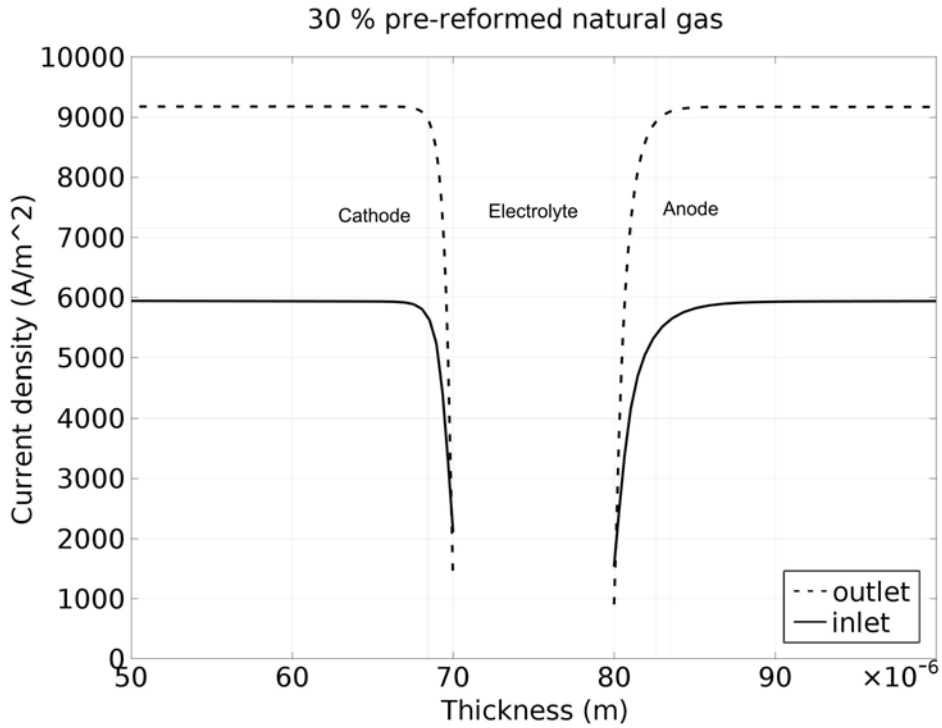

Figure 3: **Profile of electron current density at the direction normal to the main flow direction at the inlet and outlet, for the cathode, the electrolyte and the anode. Note that for the anode and cathode, only the parts (20 μm) closest to the electrolyte interface are highlighted in the figure and the "zero" is assigned at the air channel/cathode interface.**

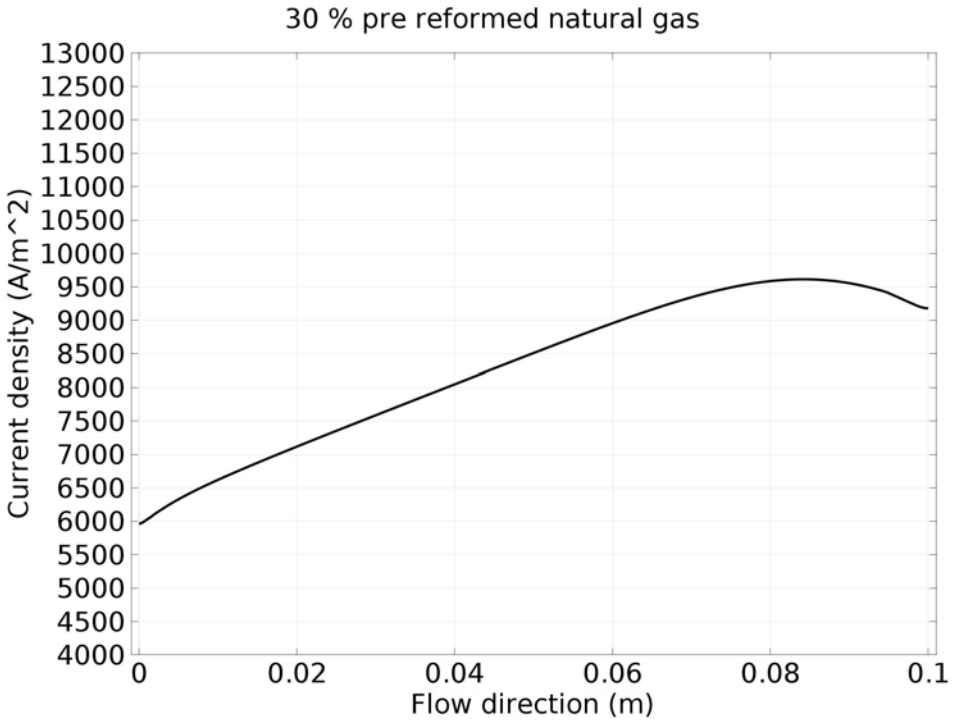

Figure 4: **The current density distribution along the main flow direction (x-direction).**

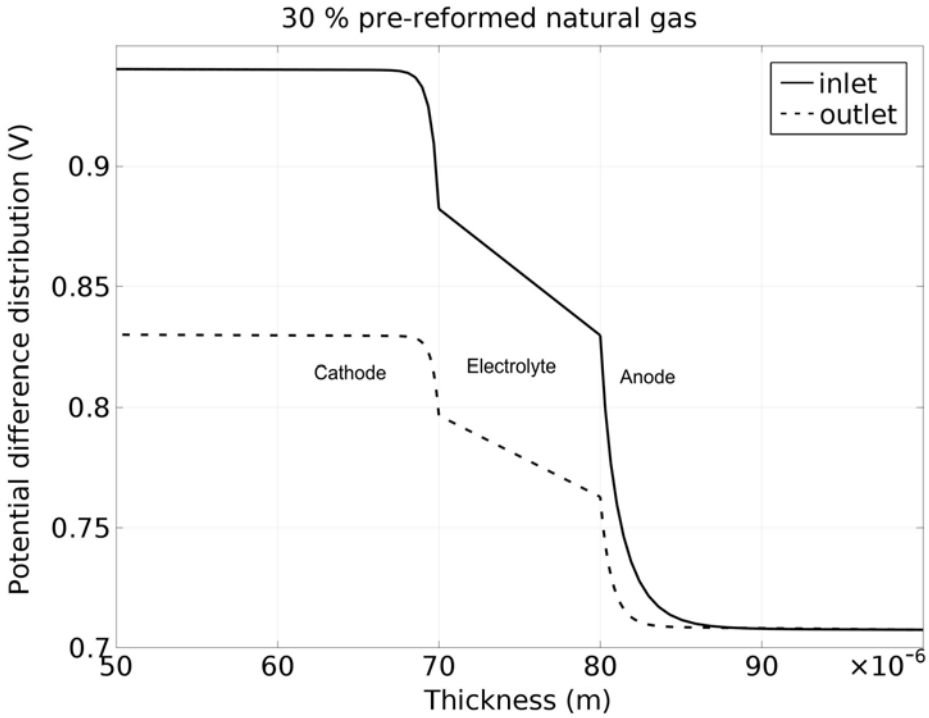

Figure 5: **The potential difference distribution in the direction normal to the main flow direction at the inlet and outlet, for the cathode, the electrolyte and the anode. Note that for the anode and cathode, only the parts (20 μm) closest to the electrolyte interface are highlighted in the figure and the "zero" is assigned at the air channel/cathode interface.**

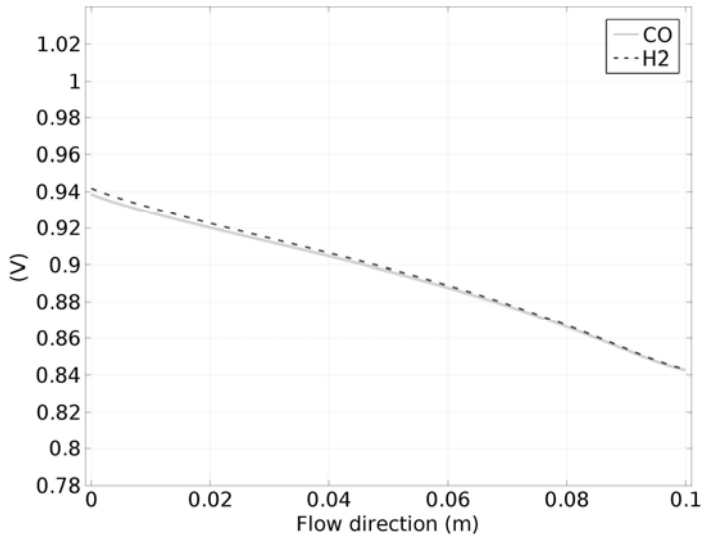

Figure 6: **The Nernst potential distribution along the flow direction for the case with 30 % pre-reformed natural gas as fuel.**

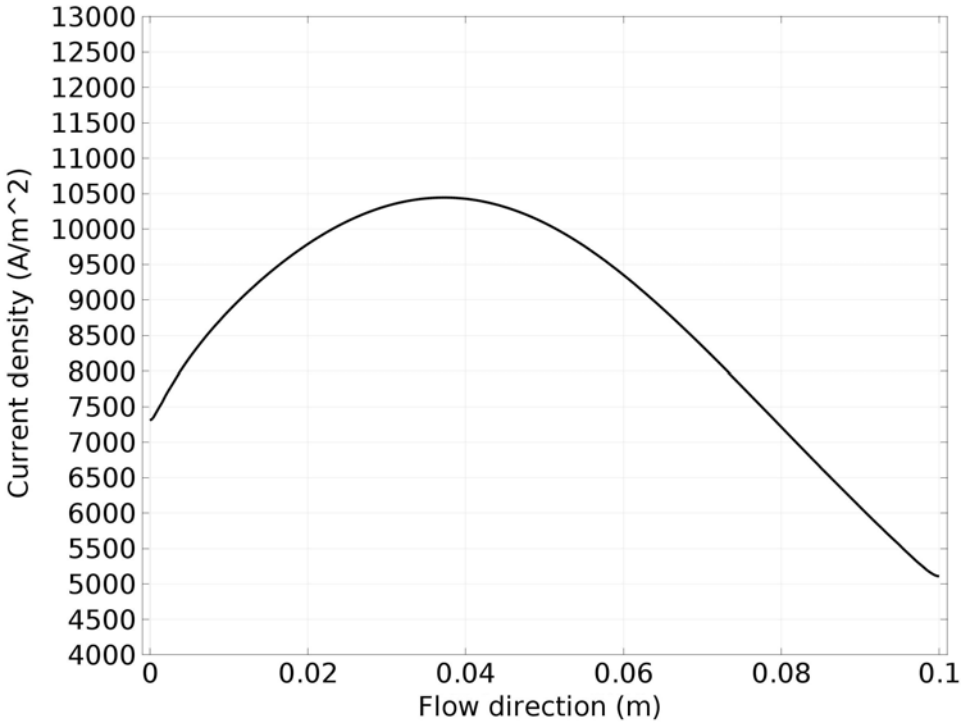

Figure 7: **The current density distribution along the main flow direction with a 1:1:1:1 mixture of hydrogen, carbon monoxide, water and carbon dioxide at the fuel inlet.**

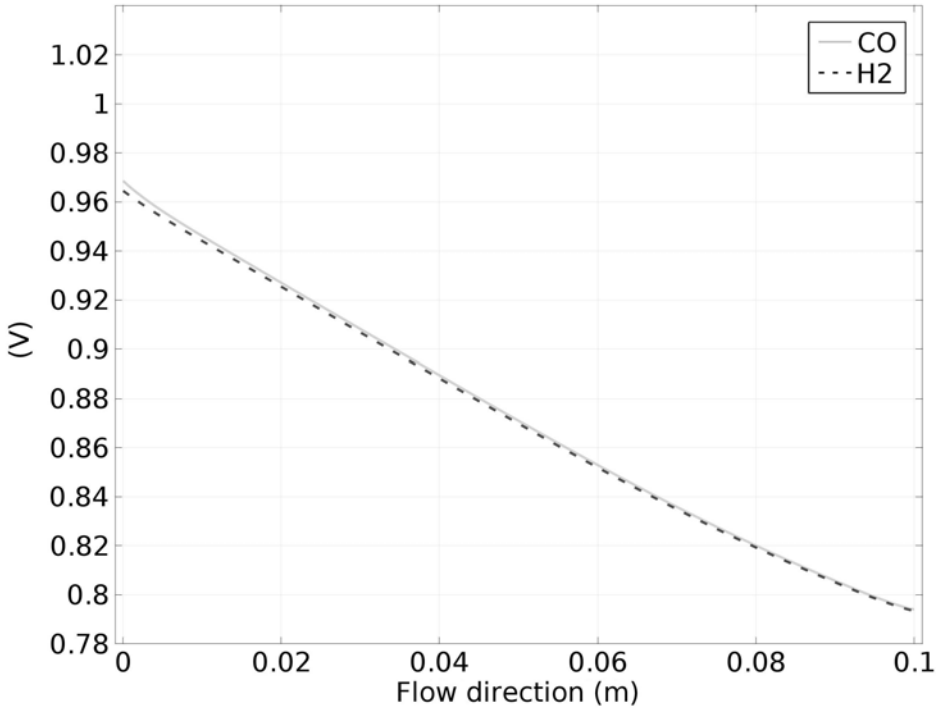

Figure 8: **The Nernst potential distribution along the main flow direction with a 1:1:1:1 mixture at the fuel inlet.**

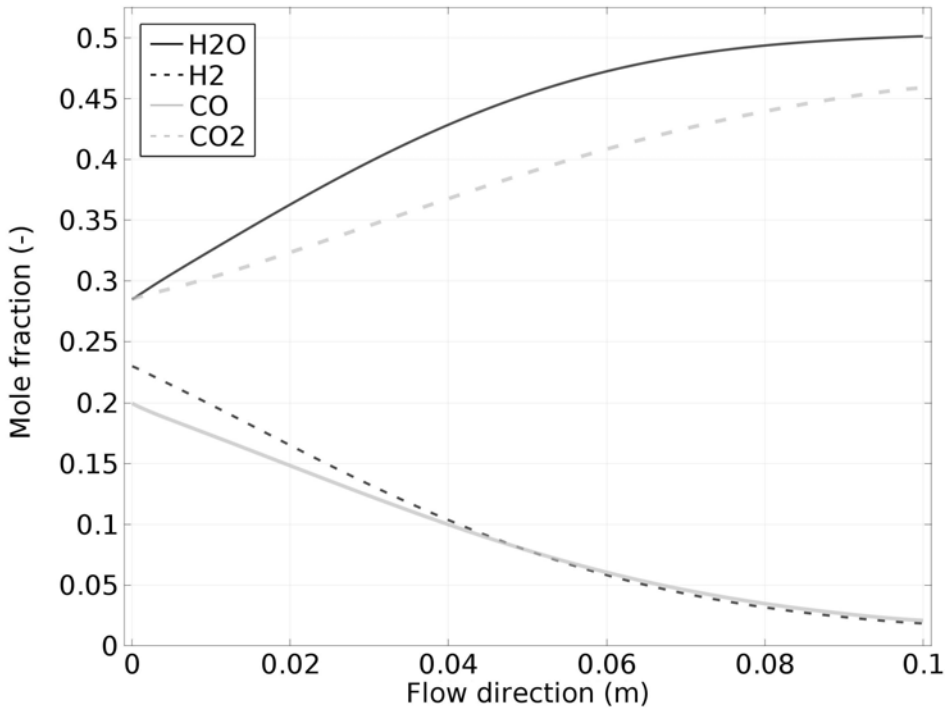

Figure 9: **The mole fraction distribution at the anode TPB along the main flow with a 1:1:1:1 mixture at the fuel inlet.**

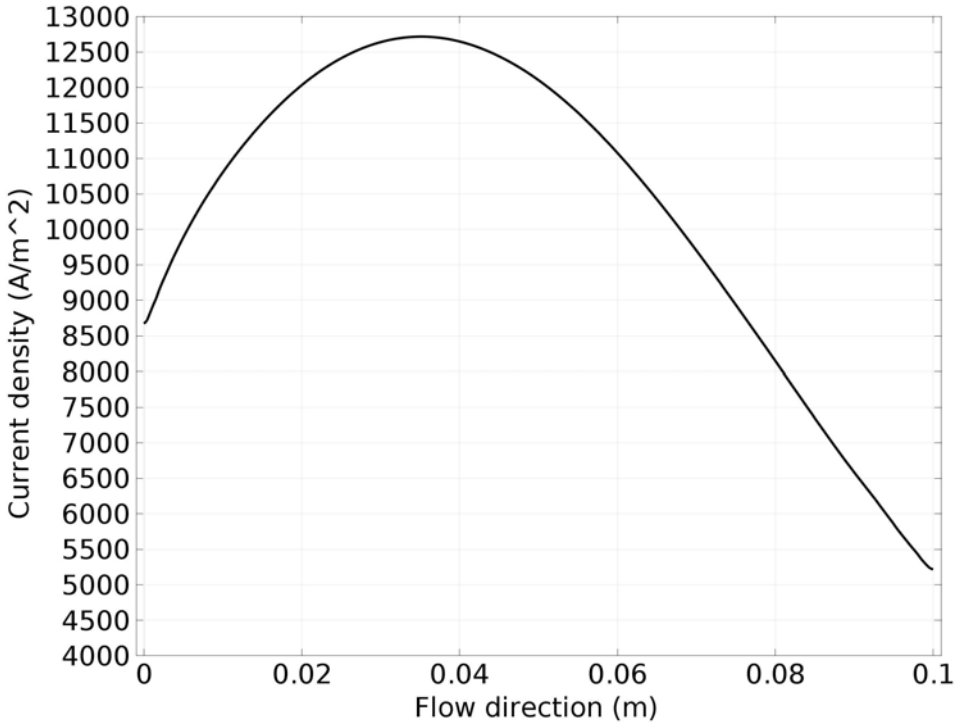

Figure 10: **The current density distribution along the main flow direction with a 4:4:1:1 mixture of hydrogen, carbon monoxide, water and carbon dioxide at the fuel inlet.**

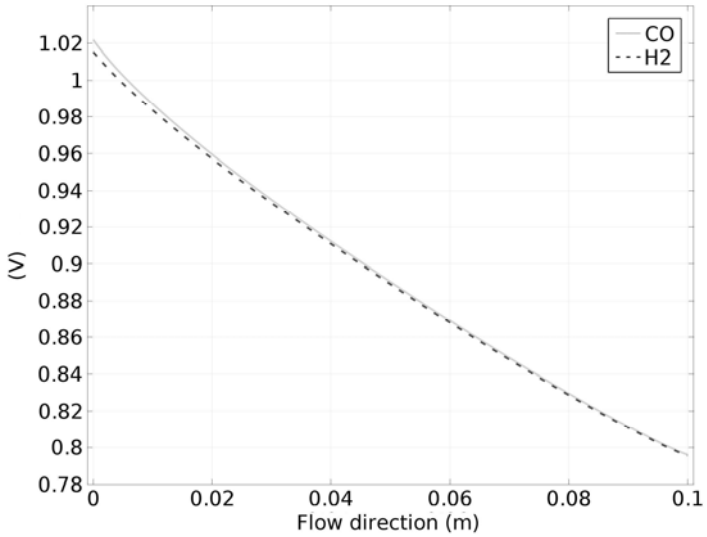

Figure 11: The Nernst potential distribution along the main flow direction with a 4:4:1:1 mixture at the fuel inlet.

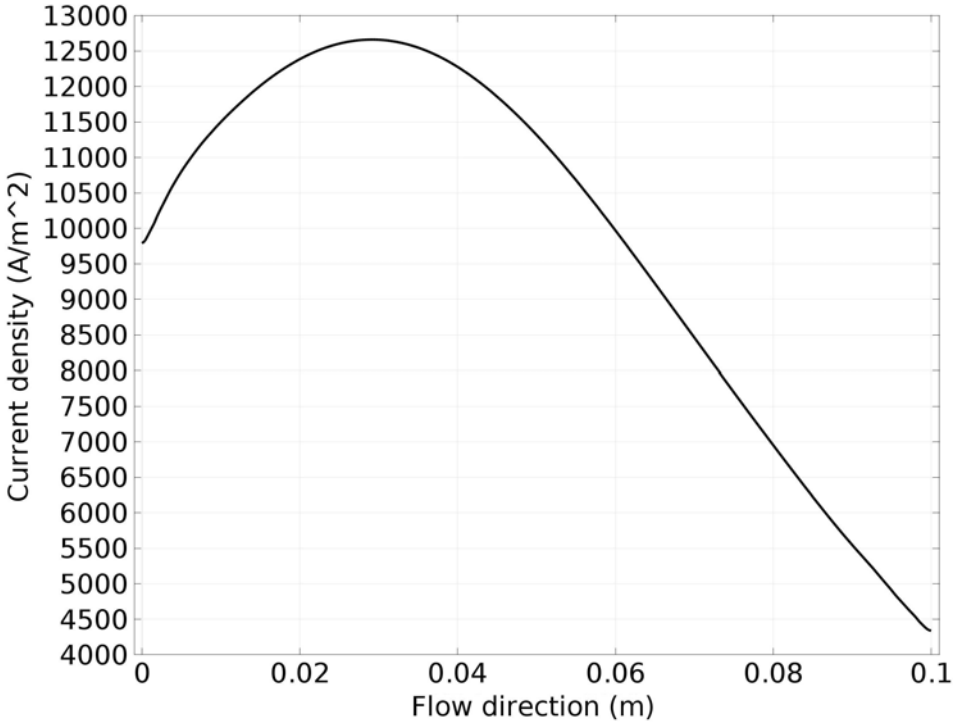

Figure 12: The current density distribution along the main flow direction with a 2:6:1:1 mixture of hydrogen, carbon monoxide, water and carbon dioxide at the fuel inlet.

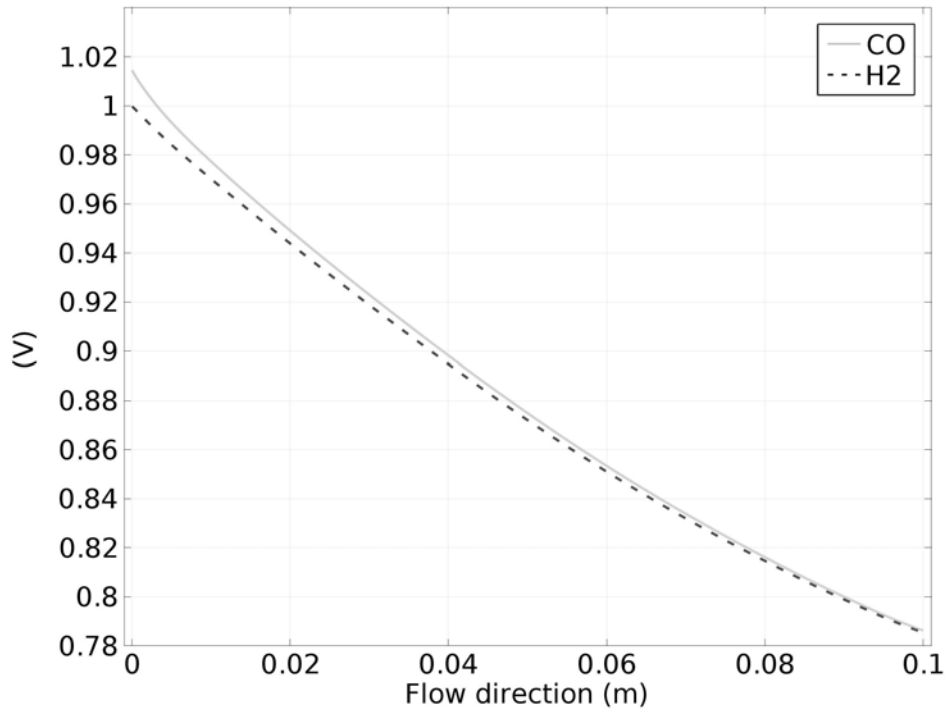

Figure 13: The Nernst potential distribution along the main flow direction with a 2:6:1:1 mixture at the fuel inlet.

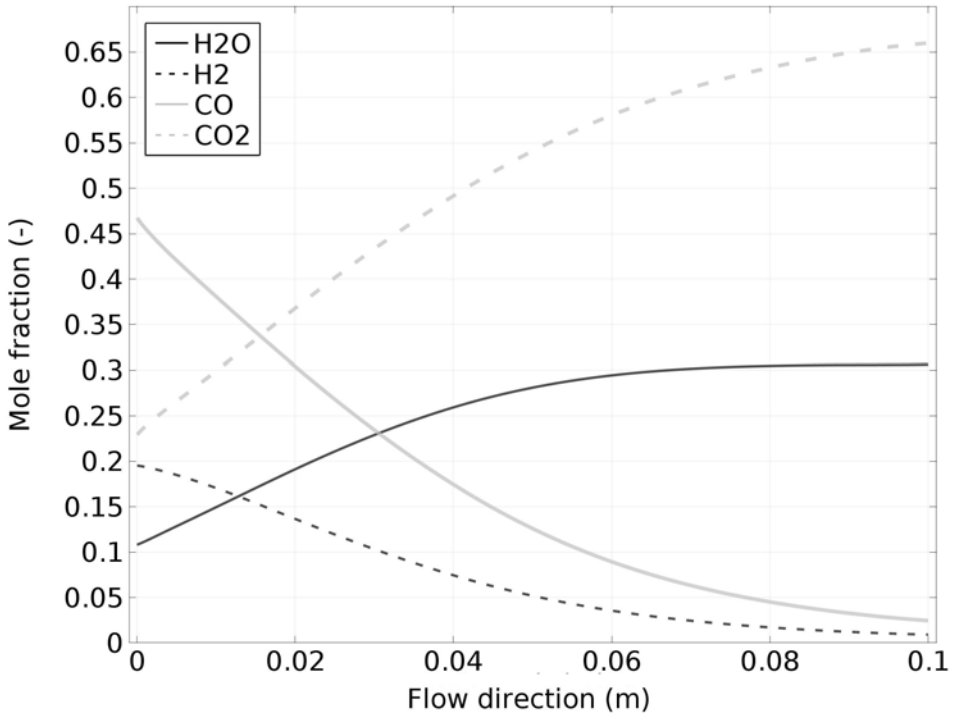

Figure 14: The mole fraction distribution at the anode TPB along the main flow direction with a 2:6:1:1 mixture at the fuel inlet.

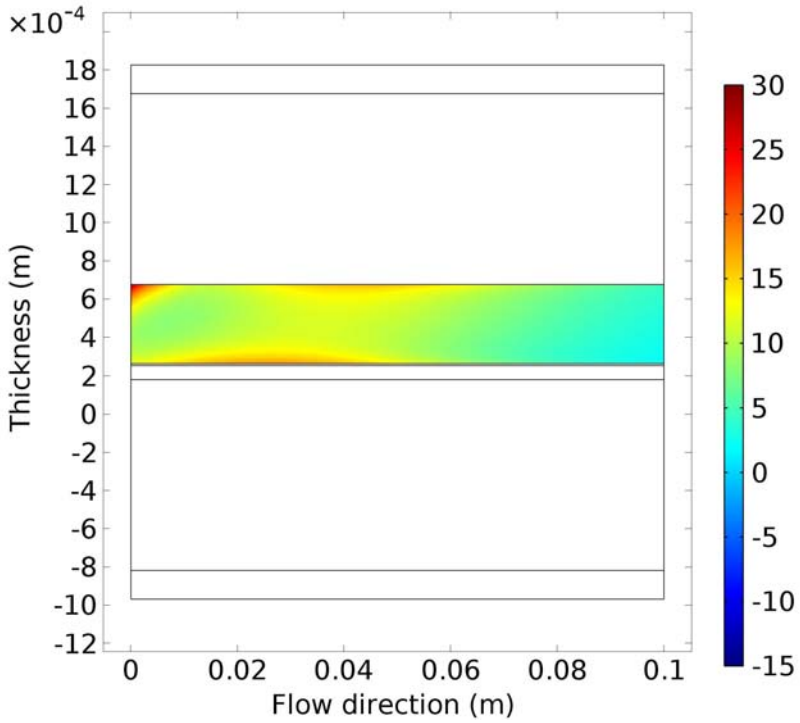

Figure 15: The WGSR rate (in mol/m^3/s), within the anode with a 2:6:1:1 mixture at the fuel inlet.

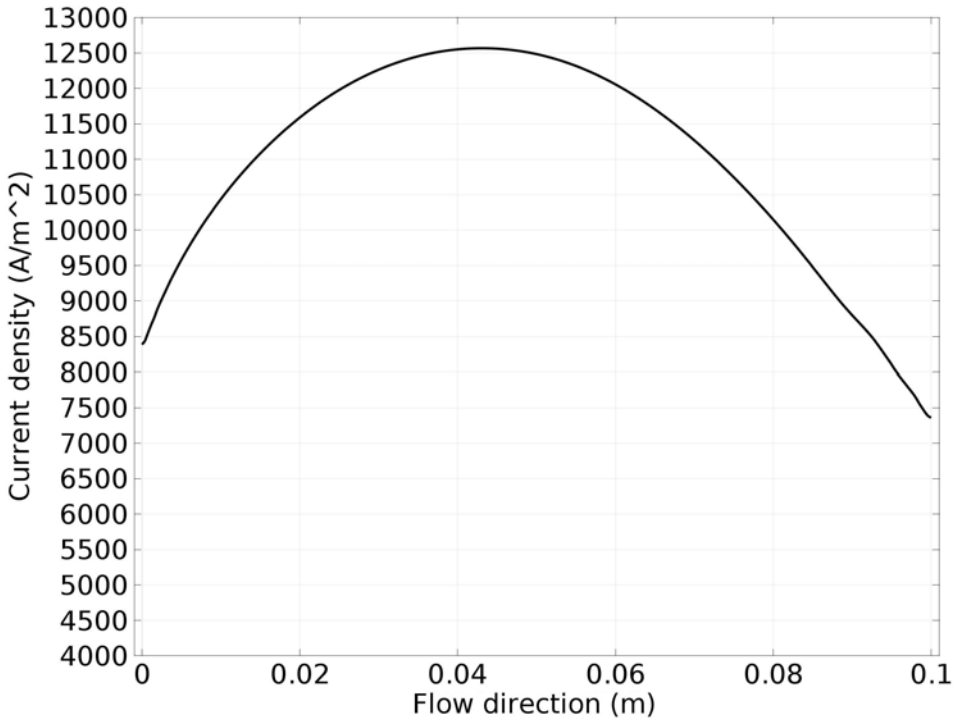

Figure 16: The current density distribution along the main flow direction with a 6:2:1:1 mixture of hydrogen, carbon monoxide, water and carbon dioxide at the fuel inlet.

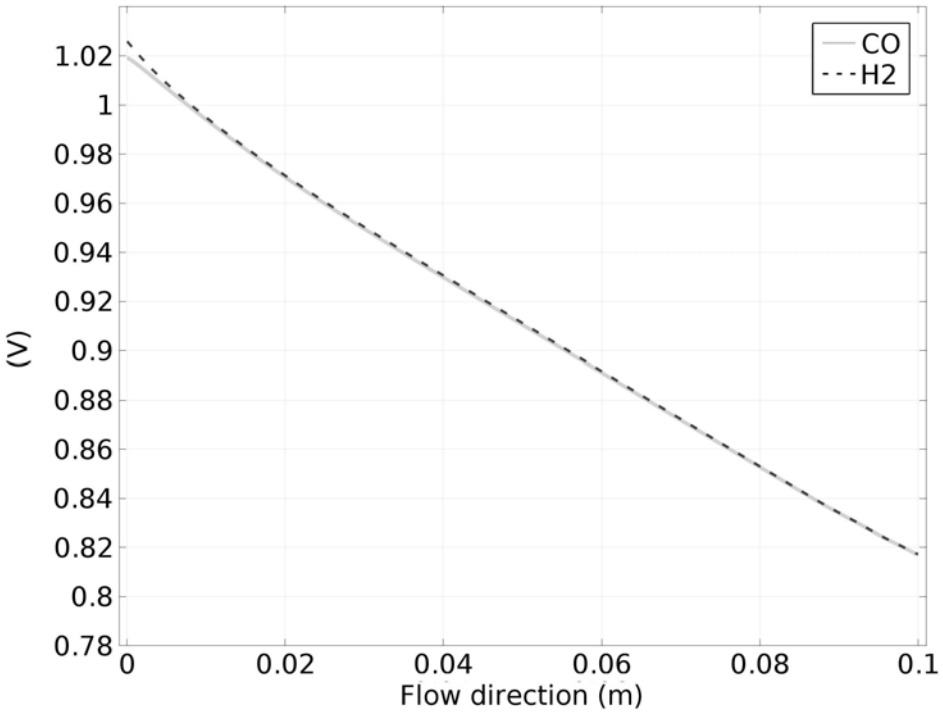

Figure 17: The Nernst potential distribution along the main flow direction with a 6:2:1:1 mixture at the fuel inlet.

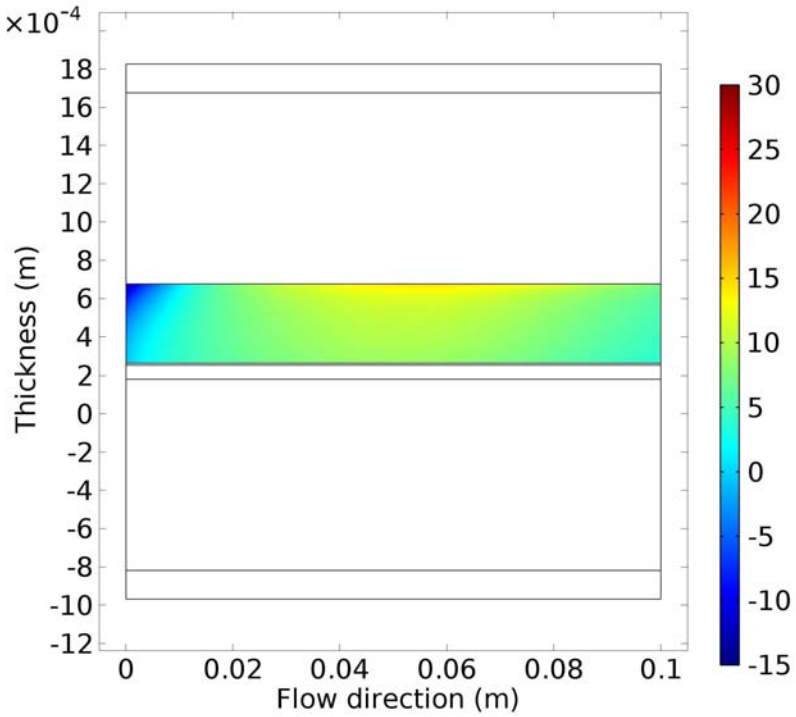

Figure 18: The WGSR rate (in mol/m^3/s), within the anode with a 6:2:1:1 mixture at the fuel inlet.

REFERENCES

[1] S. Mekhilef, R. Saidur, A. Safari, Renewable and Sustainable Energy Reviews 16 (2012) 981-989.

[2] V. Yurkiv, D. Starukhin, H.-R. Volpp, W.G. Bessler, J. Electrochem. Soc. 158 (2011) B5-B10.

[3] M. Andersson, Doctoral thesis, ISBN 978-91-7473-180-4, Lund University, Sweden (2011).

[4] M.A. Buccheri, A. Singh, J.M. Hill, J. Power Sources 196 (2011) 968-976.

[5] Y. Wang, F. Yoshiba, M. Kawase, T. Watanabe, Int. J. Hydrogen Energy 34 (2009) 3885-3893.

[6] Y. Yi, A.D. Rao, J. Brouwer, G.S. Samuelsen, J. Power Sources 144 (2005) 67-76.

[7] M. Ni, M.K.H. Leung, D.Y.C. Leung, J. Power Sources, 168 (2007) 369-378.

[8] V. Janardhanan, O. Deutschmann, J. Power Sources 162 (2006) 1192-1202.

[9] P. Leone, A. Lanzini, M. Santarelli, M. Calì, F. Sagnelli, A. Boulanger, A. Scaletta, P. Zitella, J. Power Sources 195 (2010) 239-248.

[10] K. Kendall, C.M. Finnerty, G. Saunders, J.T. Chung, J. Power Sources 106 (2002) 323-327.

[11] J.S. O´Brien, J.B. Giorgi, J. Power Sources 200 (2012) 14-20.

[12] A. Ali, X. Wen, K. Nandakumar, J. Luo, K.T. Chunag, J. Power Sources 185 (2008) 961-966.

[13] L. Liu, R. Flesner, G.-Y. Kim, A. Chandra, Fuel Cells 12 (2012) 97-180.

[14] M. Homel, T.M. Gür, J.H. Koh, A.V. Virkar, J. Power Sources 195 (2010) 6367-6372.

[15] V. Janardhanan, V. Heuveline, O. Deutchmann, J. Power Sources 172 (2007) 296-307.

[16] M.M. Hussain, X. Li, I. Dincer, J. Power Sources 161 (2006) 1012-1022.

[17] H. Miao, W.G. Wang, T.S. Li, T. Chen, S.S. Sun, C. Xu, J. Power Sources 195 (2010) 2230-2235.

[18] T.S Li, C. Xu, T. Chen, H. Miao, W.G. Wang, J. Solid State Electrochem. 15 (2011) 1077-1085.

[19] J.R. Ferguson, J.M. Fiard, R. Herbin, J. Power Sources 58 (1996) 109-122.

[20] S.A. Hajimolana, M.A. Hussain, W.M.A.W. Daud, M. Soroush, A. Shamiri, Renewable and Sustainable Energy Reviews 15 (2011) 1893-1917.

[21] Kanno D., Shikazono N., Takagi N., Matsuzaki K., Kasagi N., Electochim. Acta 56 (2011) 4015-4021.

[22] H. Iwai, N. Shikazono, T. Matsui, H. Teshima, M. Kishimoto, R. Kishida, D. Hayashi, K. Matsuzaki, D. Kanno, M. Saito, H. Muroyama, K. Eguchi, N. Kasagi, H. Yoshida, J. Power Sources 195 (2010) 955-961.

[23] N. Vivet, S. Chupin, E. Estrade, T. Piquero, P.L. Pommier, D. Rochais, E. Bruneton, J. Power Sources 196 (2011) 7541-7549.

[24] Ningbo Institute of Material Technology and Engineering (NIMTE), China.

[25] Fuel Cell Handbook (7th edition), U.S. DoE, Morgantown, West Virginia (2004).

[26] W. Winkler, P. Nehter , Fuel Cells and Hydrogen Energy 1 (2008) 15-50.

[27] M. Ni, Int. J. Hydrogen Energy 37 (2012) 1731-1745.

[28] S.B. Beale, Chapter 2 in Transport Phenomena in Fuel Cells, B. Sundén, M. Faghri (eds), WIT Press, 2005.

[29] COMSOL Multiphysics 4.3 user guide, Stockholm, Sweden (2011).

[30] Fluent 12.1 user guide, Canonsburg, Pennsylvania, USA (2009).

[31] R. Suwanwarangkul, E. Croiset, E. Entchev, S. Charojrochkul, M.D. Pritzker, M.W. Fowler, P.L. Douglas, S. Chewathanakup, H. Mahaudom, J. Power Sources 161 (2008) 308-322.

[32] M. Kemm, Doctoral thesis, ISBN 91-628-6981-7, Lund University, Sweden (2006).

[33] H. Xu, Z. Dang, B.-F. Bai, Applied Thermal Engineering 50 (2013) 1101-1110.

[34] T. Tanim, D. J. Bayless, J. P. Trembly, J. Power Sources 221 (2013) 387-396.

[35] M. le Bars, M.G. Worster, J. Fluid Mech. 550 (2006) 149-173.

[36] COMSOL Multiphysics 3.5 user guide, Stockholm, Sweden (2008).

[37] M. Andersson, J. Yuan, B. Sundén, Int. J. Heat Mass Transfer 55 (2012) 773-788.

[38] M. Andersson, J. Yuan, B. Sundén, J. Electrochemical Society, 160 (2013) F1-F12.

[39] R.C. Reid, J.M. Prausnitz, B.E. Poling, The Properties of Gases & Liquids (fourth edition), McGraw-Hill Book Company, New York, USA (1987).

[40] J. Yuan, Y. Huang, B. Sundén, W.G. Wang, Heat Mass Transfer 45 (2009) 471-484.

[41] D.Y. Murzin, T. Salmi, Catalytic Kinetics, Elsevier Science (2005).

[42] S. Kakac, A. Pramuanjaroenkij, X. Zhou, I. J. Hydrogen Energy 32 (2007) 761-786.

[43] B. Todd, J.B. Young, J. Power Sources 110 (2002)186-200.

[44] M. Andersson, H. Paradis, J. Yuan, B. Sundén, J. Fuel Cell Sci. Technol. 8 (2011) 031013.

[45] W.G. Bessler, J. Warnatz, D.G. Goodwin, Solid State Ionics 177 (2007) 3371-3383.

[46] D. Marrero-López, J.C. Ruiz-Morales, J. Peña-Martínez, J. Canales-Vázquez, P. Núñez, J. Solid State Chemistry 181 (2008) 685-692.

[47] Y. Matsuzaki, I. Yasuda, J. Electrochem. Soc. 147 (2000) 1630-1635.

[48] H. Zhu, R.J. Kee, V.M. Janardhanan, O. Deutschmann, D.G. Goodwin, J. Electrochem. Soc. 152 (2005) A2427-A2440.

[49] L. Petruzzi, S. Cocchi, F. Fineschi, J. Power Sources 118 (2003) 96-107.

[50] I. Drescher, W. Lehnert, J. Meusinger, Electrochimica Acta, 43 (1998), 3059-3068.

[51] J.-M. Klein, Y. Bultel, S. Georges, M. Pons, Chem. Eng. Sci. 62 (2007) 1636-1649.

[52] B.A. Haberman, J.B. Young, Int. J. Heat and Mass Transfer 47 (2004) 3617-3629.